



## Mesoscale Analysis of Conductive Binder Domain Morphology in Lithium-Ion Battery Electrodes

Bradley L. Trembacki,<sup>1,\*</sup> Aashutosh N. Mistry,<sup>2,\*\*</sup> David R. Noble,<sup>1</sup> Mark E. Ferraro,<sup>1</sup> Partha P. Mukherjee,<sup>2,\*</sup> and Scott A. Roberts<sup>1</sup>

<sup>1</sup>Engineering Sciences Center, Sandia National Laboratories, Albuquerque, New Mexico 87185, USA

<sup>2</sup>School of Mechanical Engineering, Purdue University, West Lafayette, Indiana 47907, USA

Typical lithium-ion battery electrodes are porous composites comprised of active material, conductive additives, and polymeric binder, with liquid electrolyte filling the pores. The mesoscale morphology of these constituent phases has a significant impact on both electrochemical reactions and transport across the electrode, which can ultimately limit macroscale battery performance. We reconstruct published X-ray computed tomography (XCT) data from a NMC333 cathode to study mesoscale electrode behavior on an as-manufactured electrode geometry. We present and compare two distinct models that computationally generate a composite binder domain (CBD) phase that represents both the polymeric binder and conductive additives. We compare the effect of the resulting CBD morphologies on electrochemically active area, pore phase tortuosity, and effective electrical conductivity. Both dense and nanoporous CBD are considered, and we observe that acknowledging CBD nanoporosity significantly increases effective electrical conductivity by up to an order of magnitude. Properties are compared to published measurements as well as to approximate values often used in homogenized battery-scale models. All reconstructions exhibit less than 20% of the standard electrochemically active area approximation. Order of magnitude discrepancies are observed between two popular transport simulation numerical schemes (finite element method and finite volume method), highlighting the importance of careful numerical verification.

© The Author(s) 2018. Published by ECS. This is an open access article distributed under the terms of the Creative Commons Attribution Non-Commercial No Derivatives 4.0 License (CC BY-NC-ND, <http://creativecommons.org/licenses/by-nc-nd/4.0/>), which permits non-commercial reuse, distribution, and reproduction in any medium, provided the original work is not changed in any way and is properly cited. For permission for commercial reuse, please email: [oa@electrochem.org](mailto:oa@electrochem.org). [DOI: 10.1149/2.0981813jes]



Manuscript submitted August 15, 2018; revised manuscript received October 3, 2018. Published October 16, 2018.

With Lithium-ion batteries (LIBs) poised to be ubiquitous in our lives,<sup>1-6</sup> from consumer electronics to automotive applications, modern electrodes must utilize reactants and lithium storage materials (active phase) as efficiently as possible, preferably maintaining high efficiency over a wide range of operating currents. Electrochemical operation of these batteries involves a combination of transport processes taking place in different phases that constitute a porous composite electrode (Figure 1). Active materials (AM), typically layered transition metal oxides such as  $\text{LiCoO}_2$  or  $\text{LiNi}_x\text{Mn}_y\text{Co}_{1-x-y}\text{O}_2$ , are the primary medium of electrochemical energy, stored in the form of intercalated lithium. Conductive additives (i.e. carbon black) facilitate electronic conduction in the solid phase as typical active materials have very poor electronic conductivity,<sup>7</sup> while non-conductive polymeric binders such as polyvinylidene fluoride (PVDF) hold the particulate components together and ascribe mechanical rigidity. The electrolyte-filled pore phase is responsible for ionic conduction of  $\text{Li}^+$  ions across the electrode to/from the separator. For electrochemical reactions to take place during battery operation, the electrochemically active AM-electrolyte interface must simultaneously have availability of intercalated Li (active material), availability of  $\text{Li}^+$  ions (electrolyte), and effective contact with an electronic pathway to the current collector. Even though the active material houses energy, finite-rate operation of LIBs relies on the close proximity of these different phases. If either the electronic pathways are not present or ionic conduction is hindered, there will be insufficient supply of reactants at the electrochemically active interface leading to a loss of performance.<sup>8-10</sup> Often the active material particles are much larger than conductive additives. Given this large disparity in length scales, one can incorporate the physicochemical interactions of these secondary solids (conductive additives and polymeric binder) in the form of a homogenized phase, referred to as conductive binder domain (CBD) hereafter.<sup>9-15</sup>

Arrangement of these multiple phases in a composite electrode mesostructure alters the efficacy of different physicochemical interactions taking place at the pore-scale and in turn results in an observable macroscale electrochemical response.<sup>16</sup> Mesostructural investigations in the context of LIBs aim to explore this intricate relationship between

mesostructural details and measurable electrode-scale behavior. Many have utilized X-ray computed tomography (XCT)<sup>17</sup> to image pore-scale electrode features with sub-micron resolution along with field-of-view dimensions close to 1 mm. As a typical active material particle size falls in between these two length-scales, XCT is quite suitable to probe associated geometrical features such as particle size distribution, spatial particle arrangement and inter-particle connectivity.<sup>18-25</sup> These studies have proved helpful in studying particle-scale effects. For example, many active materials have a non-spherical particle shape which requires commensurate improvements in understanding of Li intercalation.<sup>26-31</sup> Additionally, operational changes in particle geometry such as expansion and fracture have been probed in-operando using XCT.<sup>32-34</sup>

While XCT has provided significant insight, and imaging techniques have improved significantly in recent years, XCT still exhibits a deficiency in the context of electrode imaging: it is extremely difficult to reliably distinguish between the non-active phases in the electrode (i.e. void/electrolyte, conductive carbon additive, and binder). Given that the operability of these composite electrodes is attributed to a combination of several different material phases, the composite structures, rather than the typical AM skeleton alone, must be studied to sufficiently improve understanding of the mesostructural implications. While imaging techniques other than XCT, such as focused ion beam scanning electron microscopy (FIB-SEM) or energy dispersive X-ray spectroscopy (EDS), can clearly differentiate between the non-active phases, the field of view, or lateral image dimensions, are typically significantly smaller in published data.<sup>12,20,25,26,28,35</sup> This is likely due to the desire to obtain the highest resolution (smallest voxel size) possible, at the expense of field of view, as SEM could easily be used to image larger domains. A small electrode subdomain that spans only a few active material particles is likely not large enough to be representative of the entire electrode, but can offer insights into the morphology and location of the CBD phase. Figure 2 presents previously published images using high-resolution imaging techniques, where Figure 2a from Ebner et al.<sup>20</sup> depicts large dispersed agglomerates of CBD phase throughout the particle bed while Figure 2b from Jaiser et al.<sup>35</sup> suggests that the CBD phase might preferentially migrate to regions between particles.

To supplement the XCT information characterizing active particle network geometry, some researchers have recently developed ways to

\*Electrochemical Society Member.

\*\*Electrochemical Society Student Member.

<sup>7</sup>E-mail: [btremba@sandia.gov](mailto:btremba@sandia.gov)

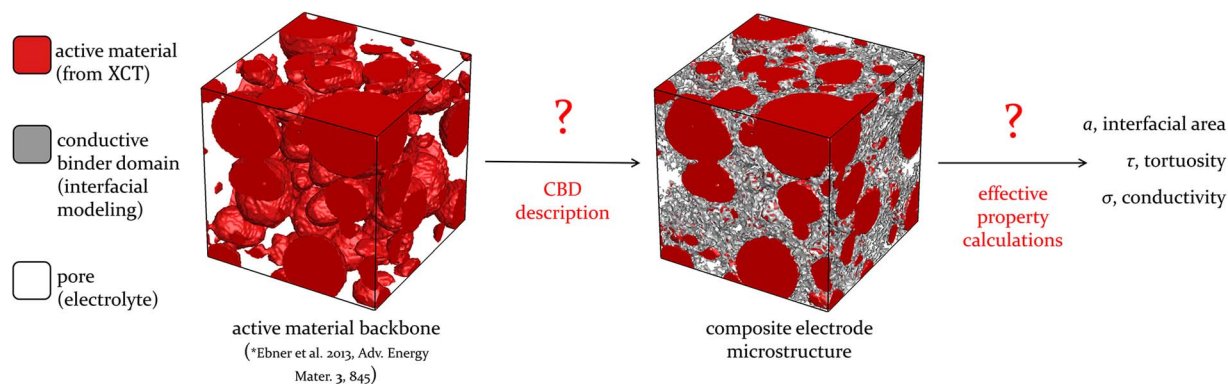


**Figure 1.** A schematic representation of the sequence of operations involved in characterizing a porous battery electrode. Tomography imaging provides details of active material distribution. The composite binder domain (CBD) description supplements this information to reconstruct composite mesostructures. The reconstructed electrode structures are then analyzed to characterize their effective properties.

introduce a CBD phase using mathematical modeling.<sup>10,12,15,25,36,37</sup> An outline of such a procedure is summarized in Figure 1. The electrode mesostructures reconstructed after these steps have all of the necessary material phases and can be analyzed to compare the effectiveness of different transport processes taking place inside such multiphase structures, expressed in terms of effective structural properties.<sup>10</sup> The process of generating a composite electrode structure and its subsequent mesostructural characterization involves various intermediate steps, and each one can affect the outcome of the analysis. In the present article, to elucidate the importance of accurate CBD morphology modeling on electrode structure, two CBD descriptions are discussed and compared: (i) Interfacial energy based<sup>10</sup> and (ii) Level-set based.<sup>15</sup> While experimental validation data is limited and typically represents behavior of materials or manufacturing recipes for which we do not have imaging data, we make comparisons to some measured electrode properties found in the literature. For a fair comparison between CBD morphology approaches, the same active material tomograph is selected. Multiple composite electrodes are realized with varying CBD morphology. The present work attempts to answer the following set of questions associated with CBD phase description in LIB composite electrodes:

1. What are the morphological differences among different CBD descriptions and how do they affect electrode-scale effective properties?
2. The CBD phase has recently been shown to contain pores of nanometer dimensions.<sup>12,25</sup> A dense CBD versus a nanoporous CBD phase could lead to different electrode structures. What sort of quantitative changes in transport characteristics will incorporating CBD nanoporosity introduce?
3. Real particles are not voxelated/stair-stepped, but tomography data is on a voxelated mesh. The voxelated data is often translated onto a body fitted mesh system for further analysis. How much structural change would this transformation introduce?
4. Prediction of effective electrode properties such as tortuosity and conductivity requires solving conservation equations. Will the method of numerical analysis introduce discrepancy in the predicted properties?

### Electrode Reconstruction Methods

As previously discussed, XCT imaging is unable to distinguish the non-active phases of the electrode mesostructure, requiring numerical techniques that introduce a composite binder phase. We present two numerical methods that address this requirement: an interfacial energy approach and a level-set approach. A high quality exemplar experimental mesostructure domain is chosen to compare the geometry reconstruction approaches.

**Experimental data.—X-Ray tomography electrode images.**—To compare numerical techniques, we selected an electrode dataset from the published XCT data by Ebner et al.<sup>20</sup> This high-quality dataset consists of image stacks for multiple NMC333 ( $\text{LiNi}_{1/3}\text{Mn}_{1/3}\text{Co}_{1/3}\text{O}_2$ ) cathodes at various binder/carbon loadings and calendaring pressures. In addition to the raw greyscale images, the authors provided binarized and labeled versions of the images, which we used for this study. We chose a  $100 \times 100 \times 60 \mu\text{m}^3$  subdomain containing more than 1000 AM particles from the 92/4/4 NMC/carbon/binder wt% loading case that was calendared at 600 bar. Figure 3a shows a stack of several binarized images with the subdomain used for this study outlined while Figure 3b depicts the 3D reconstruction of the subdomain. This subdomain is located at  $[70\text{--}170\mu\text{m}, 70\text{--}170\mu\text{m}, 5\text{--}65\mu\text{m}]$  within the dataset, which corresponds to voxel/slice ranges of  $[189\text{--}459, 189\text{--}459, 13\text{--}175]$  as each voxel is  $0.37\mu\text{m}$ . While a subdomain this large requires significant computational requirements for domain reconstruction and simulation, such a size is required to achieve behavior representative of the bulk and be considered a representative volume element (RVE).<sup>38</sup> While this domain may be representative of the bulk (and does capture nearly the entire thickness of the electrode), larger scale variations and inhomogeneities may be present and lead to differing predictions on a different sub-sample of the data.<sup>39</sup> Therefore,

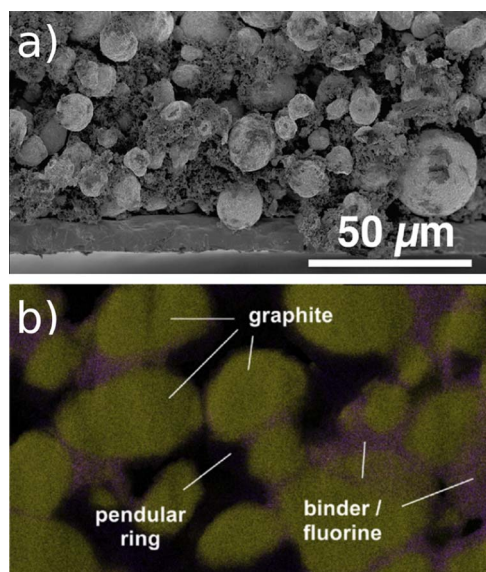


**Figure 2.** Published high-resolution images depicting various morphologies of the CBD phase within a composite electrode. Large CBD agglomerates are depicted in (a)<sup>20</sup> while migration toward regions between particles is evident in (b).<sup>35</sup>

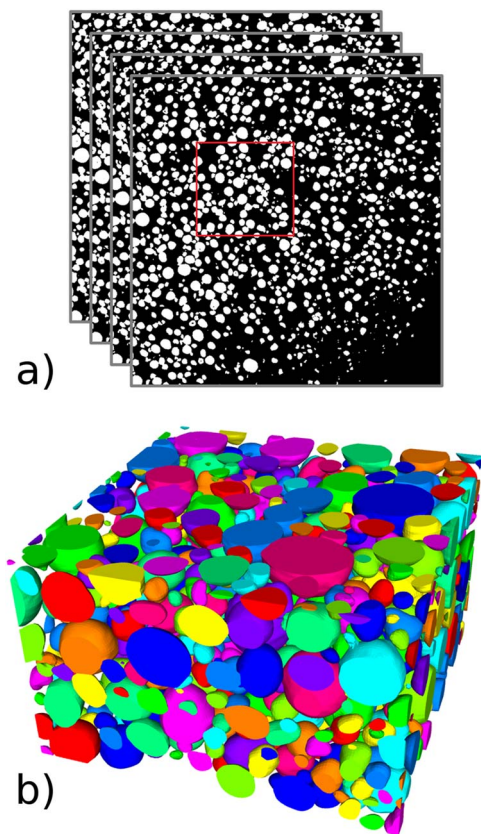


**Figure 3.** (a) A subset of the NMC cathode binarized image stack from Ref. 20 with the  $100 \times 100 \times 60 \mu\text{m}^3$  subdomain chosen for this study outlined in red and (b) the 3D reconstruction of the AM particles in the subdomain.

we were careful to use the exact same sub-domain for all calculations and comparisons in this manuscript.

**Composite binder domain.**—Using the known constituent weight fractions from the electrode manufacturing details combined with the bulk material densities, the volume of each electrode phase can be calculated. The volume fraction of the CBD phase in the electrode can be calculated with

$$\epsilon_{\text{CBD}} = \epsilon_{\text{AM}} \left[ \left( \frac{x_{\text{C}}}{1 - x_{\text{C}} - x_{\text{B}}} \right) \left( \frac{\rho_{\text{AM}}}{\rho_{\text{C}}} \right) + \left( \frac{x_{\text{B}}}{1 - x_{\text{C}} - x_{\text{B}}} \right) \left( \frac{\rho_{\text{AM}}}{\rho_{\text{B}}} \right) \right]. \quad [1]$$

The volume fraction of NMC active material is extracted from the image data ( $\epsilon_{\text{AM}} = 0.462$ ), and the density of the NMC phase is assumed to be  $\rho_{\text{AM}} = 4.7 \text{ g/cm}^3$ .<sup>20</sup>  $x_{\text{C}}$  and  $x_{\text{B}}$  represent mass fractions of carbon black and dry PVDF binder, respectively, and they are assigned the specified values of  $x_{\text{C}} = 0.04$  and  $x_{\text{B}} = 0.04$ . If we make the typical assumption of a fully dense CBD, we use bulk material density values of  $\rho_{\text{C}} = 2 \text{ g/cm}^3$  and  $\rho_{\text{B}} = 1.78 \text{ g/cm}^3$ ,<sup>20</sup> resulting in  $\epsilon_{\text{CBD}} = 0.100$ .

Although the CBD is often assumed to be dense, recent experimental work suggests that composite binder could be significantly nanoporous under typical fabrication conditions,<sup>12,25,40</sup> exhibiting measurable ionic conductivity and macroscale swelling when introduced to liquid electrolyte.<sup>12,13,25</sup> In this study we consider the effects of a CBD nanoporosity value of 47% by volume ( $\epsilon_{\text{nano}} = 0.47$ )<sup>12</sup> and a corresponding CBD ionic conductivity/diffusivity of 5% of pure electrolyte.<sup>12,25</sup> We scale the bulk density of the CBD constituents by  $\rho_{\text{np}} = \rho (1 - \epsilon_{\text{nano}})$ , resulting in nanoporous density values of  $\rho_{\text{C,np}} = 1.06 \text{ g/cm}^3$  and  $\rho_{\text{B,np}} = 0.9434 \text{ g/cm}^3$  and a corresponding value of

$\epsilon_{\text{CBD}} = 0.189$  from evaluation of (1). Consideration of nanoporosity has a large impact on our CBD reconstructions, as the assumed 47% swollen nanoporosity almost doubles CBD volume fraction when compared to the dense CBD case. Since a major role of composite binder is to provide conductive pathways through the electrode, consideration of CBD nanoporosity will likely have a large impact on predicted effective electrode properties, which we investigate in this study.

**Interfacial energy based CBD reconstruction.**—Battery electrodes are often prepared via an evaporation driven fabrication process where a colloidal slurry of solid phases loses the background solvent over time to give rise to a porous electrode microstructure.<sup>41</sup> Thermodynamically, this transition progresses toward a structure with minimum energy. Given the length scales arising in a typical battery electrode, interfacial energies dominate the energetics.<sup>42</sup> In other words, the adhesive energies of the AM-AM and CBD-CBD interfaces and cohesive energy of the AM-CBD interface dominate the microstructural evolution during electrode preparation and thus influence the final electrode structure. For a given arrangement of active material particles (such as the tomography data), the interacting factors are adhesive energy of the CBD-CBD interface and cohesive energy of the AM-CBD interface. Based on this argument, Mistry et al.<sup>10</sup> have proposed a mathematical description to reconstruct composite electrode structures from an active material backbone. This description identifies the interfacial arrangement of the CBD in terms of a morphology factor,  $\omega$  (a dimensionless descriptor ranging [0,1]). For each candidate CBD voxel (i.e., having at least one solid neighbor, AM or CBD), the deposition energy gain is expressed as

$$e_i = \frac{\omega}{6} N_{\text{CBD}} + \frac{(1 - \omega)}{6} N_{\text{AM}}, \quad [2]$$

where ‘6’ appears in the denominator to rescale energy values to lie between [0,1]. Here,  $N_{\text{CBD}}$  and  $N_{\text{AM}}$  are the number of neighboring voxels (sharing a face) that belong to the CBD or AM phases, respectively. Once the energy landscape is available for candidate CBD voxels, a finite number of voxels ( $N_{\text{candidate}}$ ) are identified for deposition based on energy values (refer to<sup>10</sup> for further details). This process is repeated until the desired  $\epsilon_{\text{CBD}}$  is achieved. If the CBD phase is nanoporous, the volume ratio AM/CBD changes accordingly.

Essentially,  $\omega$  is related to the ratio of cohesive and adhesive energies and  $\omega$  ranges from 0 to 1, with lower values leading to a film-like distribution of CBD phase over the AM surface and higher values resulting in a finger-like CBD structure on the AM backbone. Such morphological variations of the CBD phase structure alter the structural properties, resulting in different active area, tortuosity and effective conductivities as a function of morphology factor,  $\omega$ , even when the AM skeleton is unchanged.

**Level-set based CBD reconstruction.**—A reconstruction approach based on generation of a level-set field for each particle surface combined with a conformal mesh decomposition has been developed<sup>15,30,43</sup> and is summarized here for completeness. Using the commercially available Avizo software (Thermo Fisher Scientific), experimental image stacks are converted into a 3D geometry of individual particles. Each smooth particle surface is then exported as a standard tessellation language (STL) facet file. We employ the conformal decomposition finite-element method (CDFEM)<sup>44,45</sup> to convert the STL files into a computational mesh. First, a background mesh of sufficient resolution is generated and a level-set is generated for each imported particle STL file. The background mesh elements are then cut where necessary to create a mesh that conforms to the various particle level-set zero values, resulting in a conformal 3D tetrahedral mesh with very little effort required from the user.

After splitting the domain into active and non-active regions, the non-active regions must then be further divided into two regions: composite binder and void/electrolyte. The volume of the composite binder phase must match the prescribed volume of either dense or nanoporous CBD. We consider two numerical level-set approaches

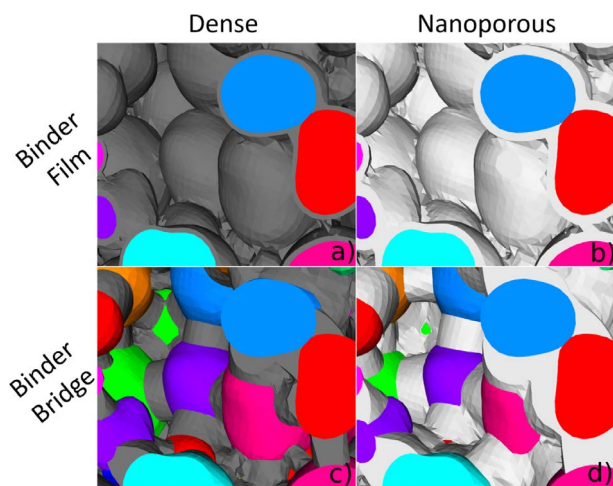


**Figure 4.** Visual comparison of the various level-set based CBD morphologies on a subset of the computational domain where particles are represented by various colors. Both (a) and (b) correspond to a uniform particle film CBD while (c) and (d) depict the binder bridge approach. Images (a) and (c) correspond to a dense CBD (dark gray) assumption, while images (b) and (d) demonstrate the increased CBD volume that corresponds to a nanoporous CBD (light gray) representation.

that result in different CBD morphologies: a uniform film approach and a bridge approach. Both have been previously described in detail.<sup>15</sup>

**Uniform binder film.**—The simplest and an often used approach to introducing composite binder into an electrode reconstruction is applying a uniform film/coating on each particle surface. This morphology roughly corresponds to a low- $\omega$  interfacial energy CBD morphology presented previously. A CBD film applied to the particles yields no particle-electrolyte area, which would have significant implications for the electrochemistry that must take place at the particle-electrolyte surface. To achieve a uniform CBD film within our level-set framework, we apply a uniform offset to the combination of the particle level-sets ( $\varphi_{P,i}$ ) into a CBD level-set ( $\varphi_{CBD, film}$ ) at every point in the domain as

$$\varphi_{CBD, film} = \min_{i=1,N} (\varphi_{P,i}) - O, \quad [3]$$

where  $O$  is the offset value that represents the film thickness and particle number  $i$  ranges from 1 to the total number of particles  $N$ . The CDFEM process splits the non-active phase of the mesh into two regions: a CBD region and an electrolyte region. For the binder/carbon loading used to manufacture this electrode, the resulting film thickness (level-set offset value) is 336nm when assuming a fully dense composite binder (Figure 4a), and increases to 643nm when assuming 47% CBD nanoporosity (Figure 4b).

**Binder bridge.**—We also consider a morphology approach that mimics high-resolution SEM imaging results where binder appears to preferentially migrate to areas near particle-particle contacts during the solvent evaporation process, forming a binder bridge between neighboring particles.<sup>28,35</sup> Preferentially placing composite binder between particles leaves some particle surface exposed to the electrolyte, allowing for a more realistic electrochemistry environment than the uniform binder film case. As in the uniform film case, we can calculate target volume fractions for both a dense and nanoporous composite binder region. We create the CBD level-set based on the combination of the individual particle level-sets at each point in the non-active mesh by

$$\varphi_{CBD, bridge} = \min_{j=1,N} \left\{ \min_{i=1,N} \left[ (\varphi_{P,i} + O) (\varphi_{P,j} + O) - S \right] \right\}, \quad [4]$$

where  $i$  and  $j$  independently range from 1 to  $N$ ,  $O$  represents a level-set offset which corresponds to binder bridge shape, and  $S$  is a parameter that dictates the size or thickness of the bridge created between particles. For a given  $O$  value (shape) choice, there is a single  $S$  value (size) that results in the correct CBD volume that we determine by iteratively generating the CBD region for a dataset and applying linear interpolation to converge on the correct  $S$  value. This method creates a level-set with negative value at points in the domain that are sufficiently close to two or more particles. The values used for parameters in the dense case are  $O = 30\mu\text{m}$  and  $S = 960.6\mu\text{m}^2$  (Figure 4c) while a nanoporous CBD requires an increase in size to  $S = 980.4\mu\text{m}^2$  (Figure 4d). It should be noted that an infinite number of unique  $O:S$  parameter combinations result in the correct CBD volume fraction. While we do not present the details here, we have studied the effect of parameter choice on morphology sensitivity and have chosen a single relatively large  $O$  value ( $30\mu\text{m}$ ) for all of our CBD reconstructions that results in sufficiently insensitive CBD shape and particle-electrolyte surface area while also resembling morphologies seen in experimental imaging results in the literature (Figure 2).

### Effective Properties of Porous Electrodes

As outlined earlier, the presence of multiple phases in a porous electrode leads to competing physicochemical interactions, the extents of which rely on intrinsic material behavior as well as relative amounts and spatial arrangement of the phases.<sup>10,46</sup> These geometrical effects can be characterized in terms of effective electrode properties: electrochemically active surface area, tortuosity, and electronic conductivity. Figure 5 highlights each of the important material phases for a typical composite electrode structure.

**Electrochemically active surface area.**—Typically, electrochemical reactions take place at the particle-electrolyte interface and represent interconversion of electronic (solid phase) and ionic (electrolyte phase) charge carriers. In LIBs, Li storage takes place in the form of intercalation. This puts an additional constraint on the associated electrochemical reaction in that it requires the presence of Li storing material (i.e., active material) at the active interface.<sup>10,14</sup> The resistance to this charge conversion is inversely related to the amount of active interface present in a given volume.<sup>47</sup> The specific active area,  $a$ , quantifies the amount of available electrochemically active interface per unit electrode volume,

$$a = \frac{\text{active interface (m}^2\text{)}}{\text{electrode volume (m}^3\text{)}}. \quad [5]$$

Note that total electrode volume is used to normalize the active interface, rather than just solid volume or active material volume. Such a definition makes the modeling of battery electrodes more intuitive<sup>48</sup> in that amount of total reaction (i.e., current) is directly proportional to specific active area (defined as in (5)) for a prescribed overpotential.

Traditionally, NMC cathode active material particles are assumed to be spherical. Assuming that all the particles are disconnected and the entire area for each is available for intercalation, active surface area per unit particle volume is  $(4\pi r^2)/(4\pi r^3/3) = 3/r$ , and equivalently specific active area per unit electrode volume is  $a = 3\varepsilon_{AM}/r$  where  $r$  is the particle radius.

**Pore phase tortuosity.**—The electrolyte phase is responsible for ionic conduction in electrochemical systems. In addition to the intrinsic electrolyte ionic conductivity, ionic conduction is governed by the porous electrode pore network arrangement. This effect is characterized in terms of porosity ( $\epsilon$ ), which is the volume of pore phase per unit electrode volume, along with tortuosity ( $\tau$ ). Porosity represents the relative volume of pore space (quantity) while tortuosity represents pore connectivity and pore network arrangement (quality). If the pore network has perfectly straight pore connections (channels), the corresponding tortuosity is unity. As these transport channels become more convoluted, the tortuosity value rises. Representative

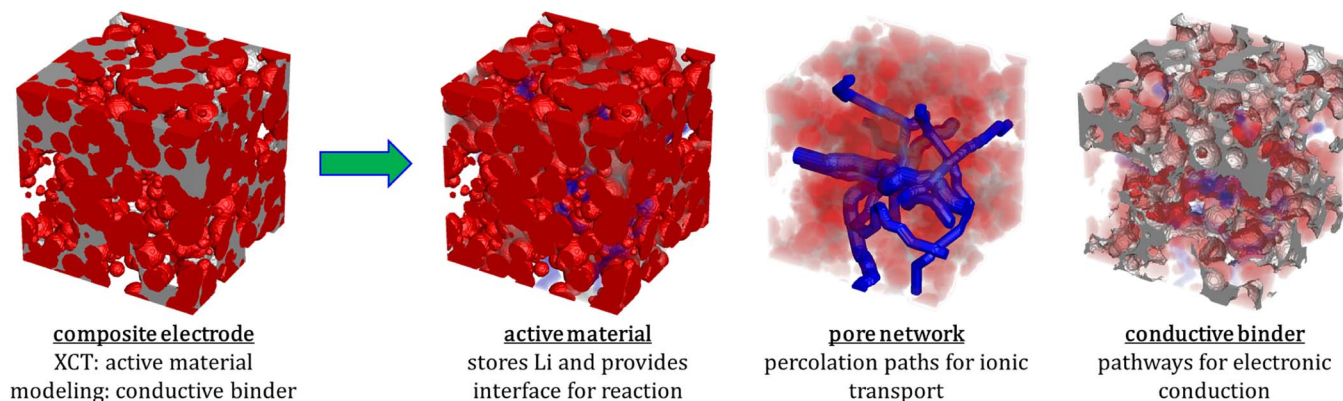


**Figure 5.** State-of-the-art porous battery electrodes have different material phases to facilitate physicochemical interactions responsible for their electrochemical performance. These schematics were generated using GeoDict (Math2Market GmbH).<sup>67</sup>

tortuous paths are presented in Figure 5. The tortuosity has a geometric interpretation,<sup>49</sup> however, a more consistent and useful definition of tortuosity is based on the solution of a steady species diffusive transport equation in a pore network, defined by the partial differential equation

$$\nabla \cdot (D\nabla C) = 0, \quad [6]$$

where  $D$  is the intrinsic electrolyte phase ionic diffusivity and  $C$  is the ion concentration.<sup>36,50–52</sup> A concentration difference is applied across the electrode by applying Dirichlet (uniform concentration) boundary conditions on two opposing boundaries while applying symmetry (no normal flux) boundary conditions on the other four boundaries.

Tortuosity  $\tau$  along the direction of interest (e.g.,  $\tau_x$  along the  $x$  direction) is defined by

$$\tau_x = \epsilon \frac{D}{D_x^{\text{eff}}}, \quad [7]$$

where the effective diffusion coefficient in the  $x$ -direction ( $D_x^{\text{eff}}$ ) is obtained from the solution of (6) and consideration of the following equations. The ion flux in the direction of interest can be defined in terms of both intrinsic diffusivity and effective diffusivity as

$$J_x = - \int_z \int_y D \frac{\partial C}{\partial x} dydz = -D_x^{\text{eff}} \left( \frac{C|_{x=L_x} - C|_{x=0}}{L_x} \right). \quad [8]$$

$J_x$  can be determined by evaluating the integral expression in (8) at any  $x$  plane in the concentration solution field resulting from the numerical solution of (6) since flux is conserved. Rearranging (8) yields the expression for effective diffusivity,

$$D_x^{\text{eff}} = \frac{-J_x L_x}{C|_{x=L_x} - C|_{x=0}}, \quad [9]$$

which then allows for a straightforward calculation of tortuosity using (7). Additional details have been provided elsewhere.<sup>10,15</sup> The electrode domain used in this study is a cuboid volume with Cartesian lengths  $L_x$ ,  $L_y$ , and  $L_z$ . Relevant intrinsic transport properties are listed in Table I.

Historically, electrode tortuosity has been assumed to be isotropic and exhibit a Bruggeman dependence on porosity,<sup>53,54</sup> i.e.,  $\tau = \epsilon^{-0.5}$ . Unlike active area, tortuosity has a directional dependence and could exhibit anisotropy based on electrode processing and/or particle shape.<sup>52</sup> Tortuosity in the other coordinate directions (i.e.  $\tau_y$  and  $\tau_z$ ) can be evaluated using equivalent forms of Equations 7–9.

**Effective electrical conductivity.**—While the pore network accommodates ionic transport, the solid phases facilitate conduction pathways for electronic transport. Most of the cathode active materials have quite poor electronic conductivity<sup>7</sup> which requires the addition of conductive carbon additives (e.g. acetylene black) to the polymeric binder. Therefore, pathways for electronic conduction are

established predominantly in the CBD (Figure 5). Since the CBD phase occupies only a small portion of the electrode volume and is spatially distributed, the electronic conductivity measured over an entire electrode volume falls well short of its intrinsic value. This apparent conductivity is more commonly referred to as the effective electronic conductivity ( $\sigma_x^{\text{eff}}$ ).

As both tortuosity and effective conductivity refer to the transport modes with similar characteristics, their calculation as well as interpretation are somewhat similar. The effective conductivity is determined based on a potential ( $\phi$ ) field solution to the steady conservation equation

$$\nabla \cdot (\sigma \nabla \phi) = 0, \quad [10]$$

where  $\sigma$  is electronic conductivity. Boundary conditions apply a potential difference across the domain similarly to the concentration difference applied when calculating ionic diffusivity. The electric current in the direction of interest ( $J_x$ ) can be defined in terms of both intrinsic conductivity and effective conductivity as

$$J_x = \int_z \int_y -\sigma \frac{\partial \phi}{\partial x} dydz = -\sigma_x^{\text{eff}} \left( \frac{\phi|_{x=L_x} - \phi|_{x=0}}{L_x} \right). \quad [11]$$

The total directional current,  $J_x$ , can again be determined by evaluating the integral expression in (11) at any  $x$  location in the potential solution field. Rearranging yields the expression for effective conductivity

$$\sigma_x^{\text{eff}} = \frac{-J_x L_x}{\phi|_{x=L_x} - \phi|_{x=0}}. \quad [12]$$

Throughout this study, we assume that the electrolyte/pore phase is not electrically conductive ( $\sigma_e = 0$ ). We assume transport across both CBD-AM interfaces and AM-AM particle contacts is ideal (no contact resistance). Refer to Table I for a list of intrinsic conductivity values. It should be noted that we apply the same experimentally measured intrinsic CBD conductivity value to both dense and nanoporous CBD as we do not have sufficient information to determine the nanoporosity of the various measurements in the literature.

Note that the traditional relations for active area and pore phase tortuosity do not account for the presence of secondary solids (CBD).<sup>10</sup> Despite this shortcoming, the traditional relations (e.g., Bruggeman) have been historically employed in LIB studies given their simplicity. Additionally, with the exception of a few studies,<sup>8,10,11,14,55,56</sup> the electronic conductivity has not been quantitatively discussed. Interestingly, the effective electronic conductivity is the easiest to measure of these three microstructural characteristics.<sup>27,50,57,58</sup>

The presence of a CBD phase increases the overall conductivity, increases the tortuosity, reduces the porosity, and alters the AM-pore interfacial area. Based on the comparison between detailed microstructure coupled electrochemical simulations and experimental tests reported in literature, Mistry et al.<sup>10</sup> recently proved that the AM-pore area behaves as the electrochemically active

**Table I. Relevant intrinsic bulk material properties of different phases constituting the composite electrode. CBD conductivity reported is specific to this carbon:binder weight ratio.**

phase	density (g/cc)	electronic conductivity (S/m)	ionic diffusivity (m <sup>2</sup> /s)
AM	4.7 <sup>20</sup>	1.039 × 10 <sup>-37</sup>	0.0
CBD	—	0.375 × 10 <sup>38,10</sup>	0.0
CBD (nanoporous)	—	0.375 × 10 <sup>38,10</sup>	0.05 <sup>12,25</sup>
C	2.00 <sup>20</sup>	—	—
B	1.78 <sup>20</sup>	—	—
pore	0.0	0.0	1.0

surface area (with three material phases, one can have three two-phase boundaries).

### Numerical Methods

One objective of this study is to quantify differences in numerical schemes when simulating transport within an electrode mesostructure. Here we introduce two numerical schemes commonly used to discretize and solve such transport equations.

**Finite volume method.**—Even though the equations governing tortuosity and conductivity are fairly straightforward, the irregular geometry resulting from different phase arrangements makes the solution challenging. Utilizing the Finite Volume Method (FVM)<sup>59,60</sup> to discretize the equations is a natural choice for transport simulation given its conservative nature and its ability to allow for a fairly convenient way of handling the phase boundaries and interface conditions. Given the voxelated nature of tomography image data, the present FVM calculations are fairly straightforward (refer to Mistry et al.<sup>10</sup> for explicit details) and are performed on a structured Cartesian grid where each computational cell corresponds to a single-phase voxel from the binarized image data. Caution should be exercised while computing the transport properties at the cell faces that reside between materials (the respective algebraic equations still remain linear).

The steady state governing equations (elliptic PDEs) are solved with appropriate transport properties in each of the material phases. As the domains investigated here are fairly large (greater than 1 million cells), the resultant linear system of equations is commensurately large. For computational efficiency over such a large matrix system, an in-house stabilized biconjugate gradient iterative linear solver is employed, and the solution is considered converged when the root mean square (RMS) correction in the solution field ( $\Delta\phi$ ) falls below 10<sup>-8</sup>. The RMS correction is defined as

$$\Delta\phi = \sqrt{\frac{1}{N} \sum_{p=1}^N (\phi_p^{new} - \phi_p^{old})^2} \quad [13]$$

where  $N$  is the total number of cells in the domain and  $\phi$  is the solution variable value at each solver iteration.<sup>10</sup>

**Finite element method.**—Another popular method used to numerically solve boundary value PDE problems is the Galerkin Finite Element Method (FEM).<sup>61</sup> We employ the FEM implementation in SIERRA/Aria.<sup>62</sup> While we typically utilize Aria on an unstructured mesh, we mostly present results from pseudo-structured Cartesian grids in this study to compare with our finite volume simulation framework that has been developed for use on structured grids/meshes. To simulate effective transport properties, we are solving steady diffusion PDEs. FEM converts each PDE to a residual equation containing both volume and surface integrals that can then be applied to the finite element mesh domain of interest, resulting in a linear sparse system of residual equations. To solve the linear systems generated by the finite element method, we utilize a generalized minimal residual method (GMRES) iterative linear solver along with an incomplete LU factorization preconditioner, which results in the numerically approximated

scalar field solution to the PDE boundary value problem. Although we do not present the details, we ensure that numerical solver tolerances are sufficient to reduce relevant errors to negligible values.

### CBD Morphology Comparison

Our hypothesis is that the level-set approaches (binder film and binder bridge) should likely correspond to, or bound, the interfacial energy approach extremes ( $\omega \rightarrow 0$  and  $\omega \rightarrow 1$ ), therefore the morphologies are presented with this in mind in all figures here. A visual comparison of several composite binder morphology approaches previously described is presented in Figure 6. We visually see that the binder film approach (Figure 6a) looks quite similar to the  $\omega = 0.01$  case (Figure 6b). At the other extreme, while we don't quite see morphology agreement between the binder bridge case (Figure 6e) and the  $\omega = 0.99$  case (Figure 6d), there does appear to be a significant formation of CBD pathways between neighboring particles, which captures the spirit of the binder bridge approach. Therefore, we expect physical behavior between these two cases to be comparable.

We present our geometric and physics results with a focus on comparing the various mesoscale CBD morphology approaches as well as comparing both dense and nanoporous CBD representations. We begin with a discussion of active area (particle-electrolyte interface area) and the implications of assuming that all particle surface area has unobstructed access to liquid electrolyte. We also present comparisons of both tortuosity and effective electrical conductivity across the various CBD representations. Both tortuosity and effective conductivity are simulated and evaluated in all three coordinate directions. For conciseness these values are presented as averaged quantities with the directional trends explained in text. In-plane directions denote the two coordinate directions parallel to the current collector boundary of the electrode, while the out-of-plane direction corresponds to the coordinate direction perpendicular to the current collector and therefore aligned with the compressive calendaring pressure applied during the manufacturing process.

In order to compare disparate meshing methods, the conformal unstructured meshes generated from the level-set CBD morphology approaches are converted to voxel-like Cartesian meshes with identical resolution as the interfacial energy method generated meshes, where each cubic computational cell/element corresponds to one voxel in the original image data (0.37 μm edge lengths). All predicted transport property results presented represent the mean between the two numerical methods used (FEM and FVM). While one might expect there to be negligible discrepancy between the two popular discretization schemes, we observed surprising discrepancies, and we discuss the comparison between the two methods in the following section focused on numerical methods analysis.

**Active area.**—The comparison of active area is presented in Figure 7 where several different y-axis scales are included. The left-most axis provides the specific particle-electrolyte active surface area ( $a$ ) value, as defined in (5). The area values presented have been corrected to account for the stair-stepped interface that a voxelated grid inherently introduces, which we discuss in detail later when discussing voxelation effects. The trends observed here are not surprising: the

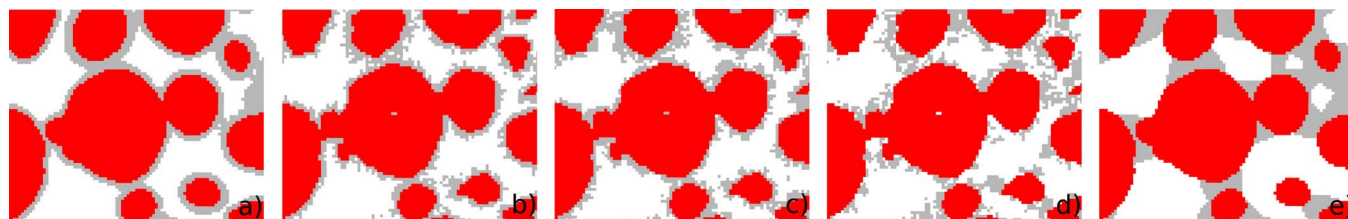


**Figure 6.** CBD morphology comparison on a 2D slice through the 3D domain depicting NMC particles (red), composite binder (gray), and void/electrolyte (white). The (a) binder film and (e) binder bridge approaches along with interfacial energy approaches corresponding to (b)  $\omega = 0.01$ , (c)  $\omega = 0.5$ , and (d)  $\omega = 0.99$  are presented.

uniform film and low- $\omega$  cases show absolutely no available surface area, since the entire particle surface is covered with composite binder and is thus not considered as active. As  $\omega$  increases, the CBD morphology trends away from a uniform film and instead extends into the pore space, corresponding to an increase in active area. Interestingly, the binder bridge approach active area falls close to an interfacial energy-based mesh with  $\omega = 0.9$ .

Assuming nanoporous composite binder increases the volume of the CBD phase and therefore results in lower values of active surface area. However, it is important to note that if the CBD is nanoporous, electrolyte will penetrate and reach the particle surface, rendering the CBD-particle area partially active. This is not, however, included in the results of Figure 7.

The second y-axis represents  $a/a_{total}$ , where  $a_{total}$  is the total AM surface area (the sum of NMC-CBD and NMC-pore interfacial areas). This axis provides a quantitative demonstration of the ratio of particle-electrolyte to particle-CBD interface area ( $a_{NMC-CBD}$ ) where the NMC-CBD area fraction ( $a_{NMC-CBD}/a_{total}$ ) is simply  $1-a/a_{total}$ . Since the CBD appears to be significantly nanoporous,<sup>12,40</sup> it is likely that in addition to NMC-electrolyte interface electrochemistry, there may be electrochemical activity taking place at the NMC-CBD interface as well (at a reduced rate due to both occluded area and diminished ionic conductivity in the CBD). Quantifying the comparative amounts of each interface type becomes important for battery models that intend to incorporate this additional pathway for electrochemical charge transfer.

The third and perhaps most important y-axis represents  $a/a_{theoretical}$ , where  $a_{theoretical}$  is the typically-used theoretical specific active area based on an average particle radius value as previously defined ( $a_{theoretical} = 3\epsilon_{AM}/r = 0.481725\mu\text{m}^{-1}$ ). We compute this value here by using an average particle radius value ( $r = 2.878\mu\text{m}$ ) that corresponds to the particle size distribution provided with this image data.<sup>20</sup> We see that using this simplified relation significantly over-estimates the active area. When nanoporous CBD is assumed, even the largest active surface area value ( $\omega = 0.99$ ) is only 20% of

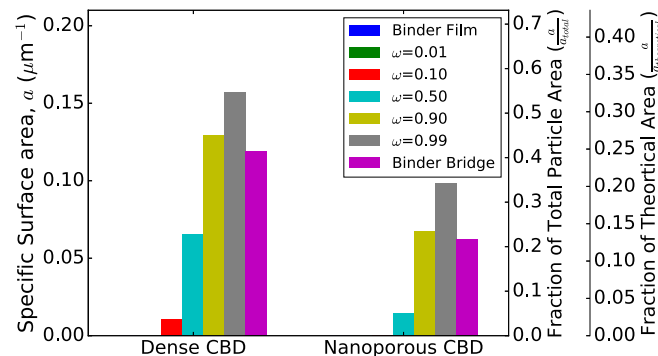


**Figure 7.** Comparison of specific active surface area across CBD morphologies, considering both dense and nanoporous CBD. Several vertical axes provide area relations relevant to large-scale battery models.

the theoretical value. There are two major sources of error: 1) using a single particle radius to represent a wide distribution of particle sizes and 2) assuming that all particle surface area is electrochemically available. Failing to account for particle-particle contact area is likely not a large source of error.<sup>15</sup>

Rather than using this typical  $a_{theoretical}$  value to approximate  $a$  for use in cell-scale battery models, a superior approach to determining an  $a$  value would be to first calculate  $a_{theoretical}$  by acknowledging the particle size distribution (rather than averaging to a single radius) and then scaling the result by the  $a/a_{total}$  values presented in Figure 7 to account for CBD particle surface coverage. For this dataset, acknowledging the particle size distribution, while still assuming spherical particles, decreases the  $a_{theoretical}$  value from  $0.481725$  to  $0.27913\mu\text{m}^{-1}$ . Using the nanoporous  $\omega = 0.99$  case as an example, this results in an improved prediction where the area value increases from 20% to 35% of the theoretical value. Further scaling by the  $a/a_{total}$  value of  $0.343$  yields an effective  $a$  value of  $0.0957\mu\text{m}^{-1}$ , which is in good agreement with the observed plotted value of  $0.0985\mu\text{m}^{-1}$ . This agreement indicates that neglecting particle-particle contact area and assuming spherical particles are likely valid assumptions when predicting active area for this dataset.

**Tortuosity.**—Tortuosity values for all CBD morphologies and treatments are presented in Figure 8. An average across the three coordinate directions is presented for each composite binder morphology and the error bars represent the corresponding spread. In all cases, the tortuosity is slightly higher (upper error bar limit) in the out-of-plane direction and lower in the in-plane directions with negligible difference between the two in-plane values. This is expected, as the calendaring process pushes particles closer together in the out-of-plane direction, resulting in more tortuous pore pathways.<sup>52</sup>

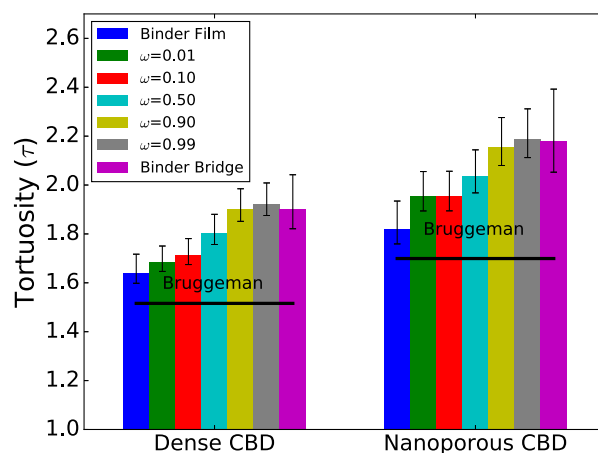


**Figure 8.** Tortuosity values across CBD morphologies. For each morphology, the colored bar represents an average across the three coordinate directions, while the error bars indicate the spread.

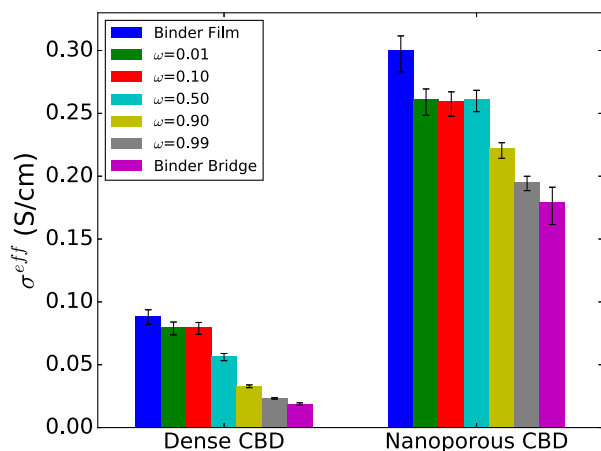


**Figure 9.** Effective electrical conductivity ( $\sigma^{\text{eff}}$ ) values for all CBD morphologies for both dense and nanoporous CBD. Here,  $\sigma^{\text{eff}}$  represents the mean across coordinate directions and error bars represent the spread.

Consideration of nanoporous CBD corresponds to higher tortuosity values (+10–17%) when compared to dense CBD as the increased volume fraction causes pathways through the pore network to be slightly more constricted. Even though a nanoporous CBD treatment necessitates allowing ionic diffusion through the CBD phase (5% of pure electrolyte value),<sup>12</sup> the limited transport through the CBD is not enough to overcome the increased CBD volume fraction.

We observe an interesting but expected trend in tortuosity values across CBD morphologies, where the level-set binder film and binder bridge approaches come close to bounding the interfacial energy approaches (and do represent bounding cases in the out-of-plane direction). We expect that the binder film and low- $\omega$  cases will behave similarly and also expect that the binder bridge approach is a worst-case scenario for tortuosity, as all particle-particle gaps are completely filled with composite binder. This well-behaved morphology comparison gives us significant confidence in our differing morphology approaches and provides a range for tortuosity that we believe can be used with confidence in larger-scale models, although it is specific to these particular electrode manufacturing parameters. We also note that all predicted values for tortuosity exceed the value predicted from the commonly used Bruggeman approximation of  $\tau = \epsilon^{-0.5}$ .<sup>53</sup>

Comparing tortuosity values calculated here with either experiments or other simulations can be difficult due to the large range of electrode manufacturing conditions possible (i.e. active material choice, particle shape/size, porosity, CBD loading, etc.). Other predictions that utilize XCT reconstructions predict values of 1.6–1.77 with some comparisons to various mixture rules, however the CBD phase is neglected, causing lower tortuosity predictions.<sup>25,51,52,63,64</sup> Our results appear to differ significantly from other binder reconstruction approaches in the literature, which predict tortuosities of ~5–11, however those electrodes exhibit significantly lower porosity than the sample studied here.<sup>25,63</sup> Experimentally measured tortuosity values (~2.75–3.5) are usually significantly larger than predicted values.<sup>26,50,64</sup> This larger experimental value may be due to a CBD morphology that is not as homogeneous as the modeled morphologies studied here, which could create significant pore blockages that dominate the tortuosity measurement.<sup>65</sup>

**Electrical conductivity.**—Figure 9 presents effective conductivity values in the same format as the corresponding tortuosity values. The bar values represent averages across the three coordinate directions with the lower bound on the error bars corresponding to the out-of-plane direction and the higher bound corresponding to the two in-plane directions. As stiff NMC particles are pushed closer together, there is less space for the polymeric binder to reside in the inter-particle gaps,

resulting in an out-of-plane conductive pathway with a comparatively lower percentage of conductive CBD, resulting in lower effective conductivity values when compared to the in-plane directions. In general, the results on this electrode reconstruction suggest that the calendering process increases tortuosity and decreases electrical conductivity in the out-of-plane (through-plane) direction.

We see that the binder bridge and binder film level-set morphologies completely bound the interfacial energy cases, and the agreement between the methods gives us confidence in the accuracy of our CBD morphology approaches. As discovered in previous studies,<sup>15</sup> departure from a CBD film morphology (low- $\omega$ ) corresponds to a decrease in electrode conductivity. This is largely due to the fact that NMC has a vastly lower intrinsic conductivity value than the composite binder, and therefore interrupting a uniform CBD film on a given NMC particle forces the particle to participate in current conduction pathways through the domain.

Perhaps the most striking observation is that consideration of nanoporous CBD significantly increases effective conductivity when compared to a dense CBD approach. Conductivity increases range from +220% (film) to +950% (bridge). This is likely due to crossing a percolation threshold between the two CBD densities, where increasing the highly-conductive composite binder volume by ~2x vastly increases the number of conductive pathways through the domain. A lower CBD nanoporosity value would yield less significant results, but may be relevant depending on measured CBD properties.<sup>25</sup>

While relevant experimental data for comparison is limited, we can compare to effective cathode conductivity studies performed on similar electrodes. Peterson and Wheeler<sup>27</sup> report values ranging from ~0.05–0.25 S/cm for LCO cathodes of varying porosity. One study investigated an electrode composed of  $\text{LiNi}_{0.8}\text{Co}_{0.15}\text{Al}_{0.05}\text{O}_2$  with a mean particle size of 10  $\mu\text{m}$ .<sup>11</sup> Although the active material is not identical, and the highest carbon:binder weight loading ratio used is 0.8:1, rather than the 1:1 ratio used here, we can still compare to the conductivity value of 0.32 S/cm. Perhaps more relevant, Lanterman et al.<sup>57</sup> report a commercial NMC523 cathode average effective conductivity of 0.201 S/cm. Our nanoporous results range from 0.16 to 0.31 S/cm which are of the same order as the experimental results, although the comparison is likely not sufficient to indicate which CBD morphology is most representative.

## Numerical Methods Analysis

We provide a discussion focused on the impact of numerical method choices. We compare results from FVM and FEM simulations and also discuss how the differences between Cartesian voxelated meshes and body-fitted conformal meshes can affect electrode property predictions.

**Discretization method: FEM vs. FVM.**—Here we present and discuss numerical solution method comparisons (FEM vs. FVM) on the various electrode reconstructions previously discussed. While the goal of this study is to collaboratively compare differing mesoscale CBD morphology representations, a comparison of numerical techniques was required to understand our results and highlights very interesting behavior. To perform the comparison, the same boundary conditions and governing equations were applied to the exact same mesh/grid geometries in both Sandia's SIERRA/Aria FEM framework<sup>62</sup> and the Purdue group's in-house FVM framework.

Figure 10 and Figure 11 present both mean tortuosity and effective conductivity results with a focus on numerical method comparison. All values plotted are means across the three coordinate directions, as there were no significant differences between the directions when comparing numerical methods. The colored bar values represent the average across the two numerical methods and the error bars represent the spread. In Figure 10, the upper error bar value corresponds to FVM results, while the lower bound corresponds to FEM. In Figure 11, the trends are the opposite (FVM predicts significantly lower values than FEM).

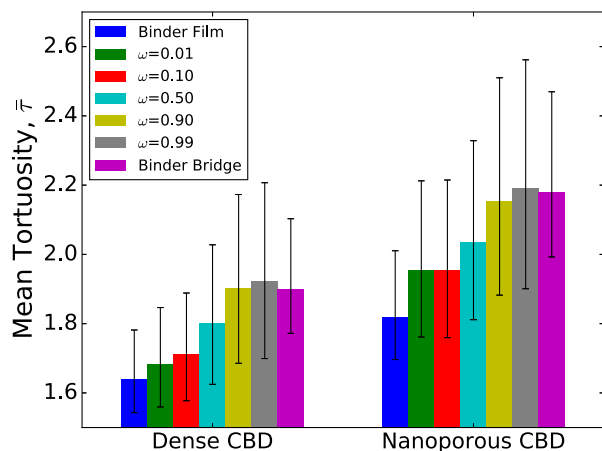


**Figure 10.** Comparison of tortuosity values predicted by both FVM and FEM numerical methods. The bar value represents the mean between the two methods while the error bar extremes represent the predicted values from FVM (top) and FEM (bottom).

It is important to note that the numerical differences are not insignificant. For both tortuosity and effective conductivity, the differences between numerical approaches is on the same order as (or larger than) the differences between the various CBD morphologies. This is a significant finding that has implications to all mesoscale transport simulation efforts in the field, particularly when comparing results in the literature using different numerical methods, and these results highlight the necessity for thorough solution verification.

While such a large discrepancy between numerical methods is not expected, we believe the results are legitimate, and we provide our justification in the Appendix. The unexpected behavior is due to the singularity-like condition when two high-conductivity elements/cells only touch at an edge/corner. While this issue is exacerbated by using a voxelated (Cartesian) grid where corner and edge conductive phase connections are expected, there is no guarantee that such a condition is entirely avoided when using conformal and/or unstructured grids, although the error would likely be significantly reduced. Ideally, a smart meshing approach that refines the mesh in elements/cells with high current density would need to be employed to limit these types of numerical errors.<sup>38</sup> At minimum, an indicator of a singularity-like

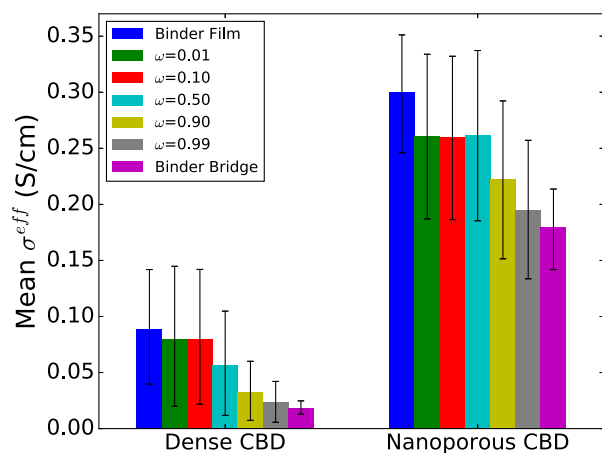


**Figure 11.** Comparison of effective conductivity values predicted by both FVM and FEM numerical methods. The bar value represents the mean between the two methods while the error bar extremes represent the predicted values from FVM (bottom) and FEM (top).

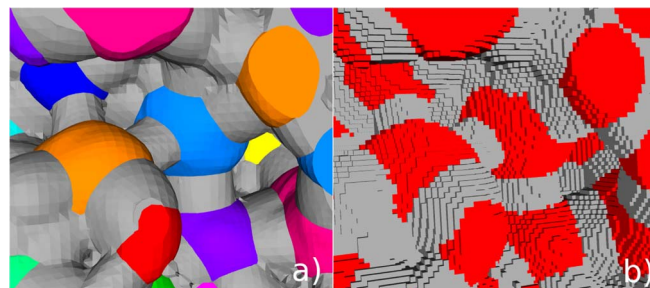


**Figure 12.** Visual comparison of (a) a conformal binder bridge mesh and (b) the morphology after converting the mesh to a Cartesian grid. The void/electrolyte mesh is not included in the image, but composite binder (gray) and NMC particles (various colors) are shown.

condition in the conduction pathway would be useful for detecting when a mesh may be introducing significant numerical error.

**Voxelation effects.**—As previously mentioned, the conformal meshes generated by the level-set reconstruction approach were converted to voxelated Cartesian meshes for accurate comparison with the meshes generated by the interfacial energy algorithm. The voxelated mesh resolution was matched to those meshes, which themselves use the XCT imaging technique resolution. Each cell in the 3D voxelated grid was assigned a material phase based on the material phase located at the element's centroid in the conformal mesh. Figure 12 provides a visual representation of the voxelation process result, where we see no significant change in overall morphology, aside from the expected stair-stepped (digitized) surface.

We present the error in the voxelated mesh relative to its conformal counterpart in Table II. Phase volumes are not included in the table, as there were negligible differences in volume. Both in-plane and out-of-plane results for the physics simulations (tortuosity and effective conductivity) all showed relatively small differences, so the mean error is reported.

We observe a small and consistent difference of only a few percent in tortuosity values, independent of CBD morphology or density. There is a significant decrease in effective electrical conductivity after voxelation, especially for the dense CBD cases. We again see the importance of considering nanoporous composite binder, as the relative voxelation error in conductivity is significantly reduced when comparing to the corresponding dense case. As with the morphology comparison above, this is likely due to the morphology being near a percolation threshold, and voxelating the CBD significantly reduces continuous conduction pathways as thin morphology features are lost or become discontinuous.

Interfacial area calculation based on voxelated information is somewhat challenging as the assigned material phase means that the voxel centroid has that phase. This does not explicitly mean that the voxel-voxel common plane is the two phase boundary. A specialized algorithm (modified Minkowski)<sup>10</sup> has been employed here to properly account for the various two phase interfaces and associated area measure. This method takes into consideration the phase information

**Table II.** Error percentages in voxelated level-set meshes relative to their corresponding conformal meshes. Area comparisons are made after surface area correction factor from Mistry et al.<sup>10</sup> is applied.

Morphology	CBD Density	$\tau$	$\sigma^{eff}$	$a$
Binder Film	Dense	2.7	−10.9	-
Binder Film	Nanoporous	2.9	−6.8	-
Binder Bridge	Dense	2.7	−16.1	6.1
Binder Bridge	Nanoporous	2.3	−8.8	9.6

of the adjoining voxels in order to virtually reconstruct the interface. Later on this value is compared with a reference geometry (e.g., digitized sphere) to calculate area. With this measure the total particle surface area estimates are within 1% of the conformal mesh value, thus confirming the acceptable fidelity of area calculation methods across the two realizations. Interestingly, the voxelated particle-electrolyte surface area,  $a$ , is still significantly increased (6.1–9.6%) when compared to the conformal representation. This clearly points to the altered CBD phase geometry as a result of voxelation.

### Conclusions

In this paper, we presented and compared various composite binder domain (CBD) morphologies resulting from two different CBD reconstruction models. These models are necessitated by the inability to image large porous electrode samples while resolving the location of the CBD within the particle network. We consider both a binder film morphology as well as a binder bridge morphology that result from a level-set based model. Additionally, five distinct morphologies resulting from an interfacial surface energy based model are also considered. The resulting geometries are discussed, with a focus on particle-electrolyte surface area. We also utilize both the finite volume method (FVM) as well as the finite element method (FEM) to simulate mesoscale electrical and ionic transport through the various material phases present in the porous electrode reconstructions. Analyzing these electrode properties across multiple reconstructions allows us to compare completely independent and unique CBD morphology modeling approaches for the first time. These reconstruction methods could theoretically be applied to any electrode image dataset that can be reliably binarized, although the binder bridge method does require the ability to distinguish individual particles.

This collaborative comparison allows us to confidently draw several conclusions about mesoscale reconstructions and how they can inform larger-scale battery models. Our in-depth discussion of electrochemically available surface area highlights the necessity to both acknowledge particle size distribution as well as account for CBD blockage of particle surfaces when calculating a specific active area ( $a$ ) value to use in a typical cell-scale porous electrode theory battery model. Predicted transport properties show good agreement between the two CBD model approaches and behave as expected. We show a general trend that moving away from a uniform film type of CBD morphology results in increased tortuosity and decreased effective electrical conductivity. We also see a significant anisotropy in both electrode transport properties with decreased transport (decreased conductivity, increased tortuosity) in the out-of-plane (through-plane) direction.

We discuss the often neglected topic of numerical methods effects with a focus on the different behavior of FVM and FEM simulations on the same mesh, where simulation predictions can differ by as much as an order of magnitude. We see very significant and unexpected discrepancies between the two methods and demonstrate that conduction through singularity-like points between conductive materials is likely the cause. This finding highlights the need for numerical verification in these types of simulations and suggests that advanced methods such as adaptive meshing may be necessary when simulating transport, especially on Cartesian/voxelated grids. We also briefly compare predicted effective properties on both conformal (smooth) meshes to voxelated meshes, noting an increase in tortuosity and active area along with a decrease in conductivity upon voxelating a conformal mesh.

While we have demonstrated the agreement between CBD reconstruction models and established a range of possible morphologies, the models would benefit from both further characterization of intrinsic material properties as well as experimentally measured effective properties (area, tortuosity, conductivity) on electrodes that have corresponding high-quality XCT data. An additional effective electrode property that would be of interest to cell-scale models is

the effective mechanical modulus, especially if macroscale swelling or mechanical abuse scenarios are of interest. Additionally, applying these reconstructive methods to a wider range of electrode XCT data on many electrodes is an avenue for near-term future work that would provide insights into how manufacturing decisions can affect pore-scale properties that ultimately lead to macro-scale battery performance.

### Acknowledgments

We appreciate Vanessa Wood's group at ETH Zurich for publishing their experimental mesostructure image stacks online. This work was funded by the U.S. Department of Energy (DOE) Vehicle Technologies Office CAEBAT III program led by Brian Cunningham at DOE. Sandia National Laboratories is a multi-mission laboratory managed and operated by National Technology and Engineering Solutions of Sandia, LLC., a wholly owned subsidiary of Honeywell International, Inc., for the U.S. Department of Energy's National Nuclear Security Administration under contract DE-NA0003525. This paper describes objective technical results and analysis. Any subjective views or opinions that might be expressed in the paper do not necessarily represent the views of the U.S. Department of Energy or the United States Government.

### Appendix

**FEM vs. FVM: A comparative verification case study.**—The discrepancy between simulation results from the finite element method (FEM) code and finite volume method (FVM) code were so extreme that more investigation was warranted. A simple case study is considered, consisting of a two-dimensional two material checkerboard with significantly differing intrinsic conductivities ( $\sigma_1 = 1$ ,  $\sigma_2 = 0.01$ ). The effective conductivity through such a geometry, depicted in Figure A1, has been previously studied and equates to  $\sigma^{\text{eff}} = \sqrt{\sigma_1\sigma_2} = 0.1$ .<sup>66</sup> However, simulating transport across the geometry with the rigorously verified Sierra/Aria framework (FEM) and the commercial ANSYS/Fluent platform (FVM) yields  $\sigma^{\text{eff}}$  values of 0.383 and 0.0234, respectively, demonstrating over an order of magnitude disagreement between the methods. This setup of one finite element/volume per block/voxel of material is representative of the previously presented simulation results, suggesting that numerical discretization limitations are the cause of the discrepancy in the predicted electrode effective transport properties that we observed.

A mesh refinement study was performed on the 2D checkerboard by uniformly refining the 2D mesh while maintaining the geometry, as shown in Figure A1, where a total of 8 successive mesh refinements were applied. The results of the refinement study are shown in Figure A2, where we observe that both methods do show convergent behavior toward the exact solution, but converge extremely slowly ( $\sim 1/4$  order), considering they both employ a 2<sup>nd</sup> order spatial discretization scheme. Both selective mesh refinement or higher-order numerical schemes may alleviate the numerical limitations observed here, but that investigation is left for future work. Voxelated meshes and highly dispersed phases will amplify the numerical errors. This case study highlights the importance of quantifying numerical error and suggests that care be taken when comparing numerical analysis results that employ different methods.

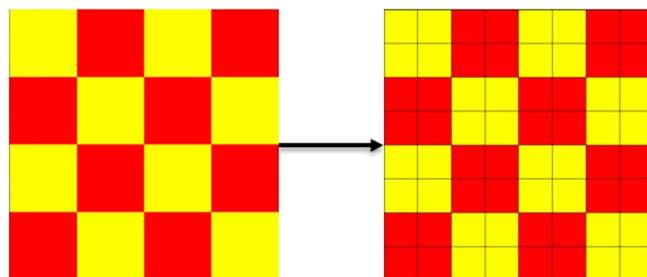


**Figure A1.** Depiction of 2D checkerboard meshed geometry with both one finite element/volume per material domain (left) and after one uniform mesh refinement (right).

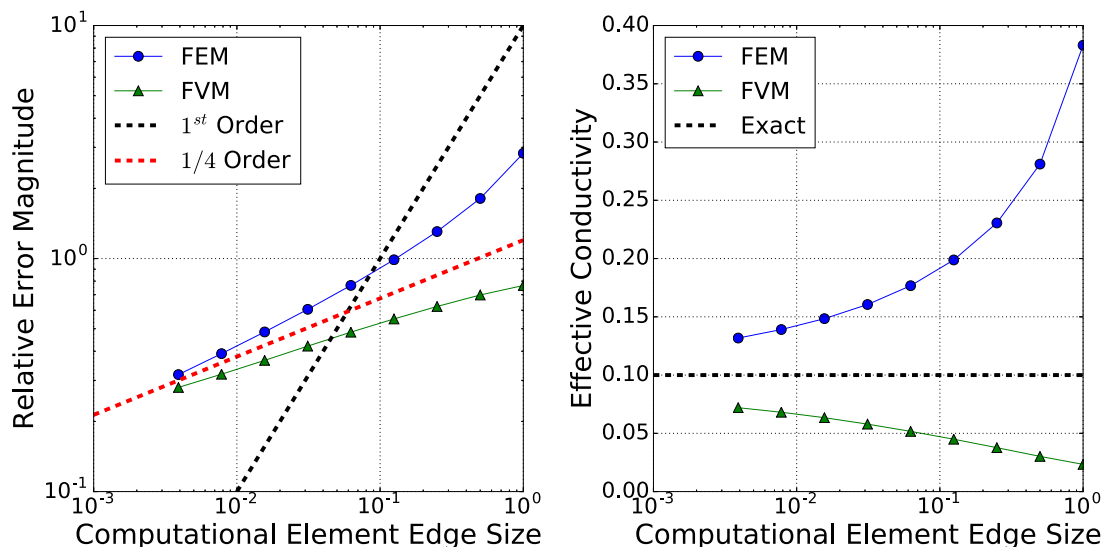


**Figure A2.** Uniform mesh refinement behavior of the 2D checkerboard case study. Relative error in  $\sigma^{\text{eff}}$  value and corresponding order of convergence (left) as well as absolute value for  $\sigma^{\text{eff}}$  (right) are plotted versus computational element edge length. The largest edge length plotted corresponds to one voxel/element/cell per material block in the checkerboard pattern.

### ORCID

Bradley L. Trembacki <https://orcid.org/0000-0001-8742-3679>

Aashutosh N. Mistry <https://orcid.org/0000-0002-4359-4975>

Scott A. Roberts <https://orcid.org/0000-0002-4196-6771>

### References

- S. M. Whittingham, *Chem. Rev.*, **104**(10), 4271 (2004).
- M. Armand and J.-M. Tarascon, *Nature*, **471**(7179), 652 (2008).
- E. J. Carins and P. Albertus, *Annu. Rev. Chem. Biomol. Eng.*, **1**, 299 (2010).
- V. Etacheri, R. Marom, R. Elazari, G. Salitra, and D. Aurbach, *Energy Environ. Sci.*, **4**(9), 3243 (2011).
- J.-M. Tarascon and M. Armand, *Mater. Sustainable Energy*, 171 (2011).
- A. Manthiram, *J. Phys. Chem. Lett.*, **2**(3), 176 (2011).
- M. Park, X. Zhang, M. Chung, G. B. Less, and A. M. Sastry, *J. Power Sources*, **195**(24), 7904 (2010).
- G. Liu, H. Zheng, S. Kim, Y. Deng, A. M. Minor, X. Song, and V. S. Battaglia, *J. Electrochem. Soc.*, **155**(12), A887 (2008).
- H. Zheng, J. Li, X. Song, G. Liu, and V. S. Battaglia, *The J. Phys. Chem. C*, **116**, 4875 (2012).
- A. N. Mistry, K. Smith, and P. P. Mukherjee, *ACS Appl. Mater. Interfaces*, **10**(7), 6317 (2018).
- G. Liu, H. Zheng, X. Song, and V. S. Battaglia, *J. Electrochem. Soc.*, **159**(3), A214 (2012).
- L. Zielke, T. Hutzenlaub, D. R. Wheeler, C.-W. Chao, I. Manke, A. Hilger, N. Paust, R. Zengerle, and S. Thiele, *Adv. Energy Mater.*, **5**(5), 1401612 (2015).
- S. Vierrath, L. Zielke, R. Moroni, A. Mondon, D. R. Wheeler, R. Zengerle, and S. Thiele, *Electrochem. Commun.*, **60**, 176 (2015).
- A. Mistry, D. Juarez-Robles, M. Stein, K. Smith, and P. P. Mukherjee, *J. Electrochem. Energy Convers. Storage*, **13**(3), 031006 (2016).
- B. L. Trembacki, D. R. Noble, V. E. Brunini, M. E. Ferraro, and S. A. Roberts, *J. Electrochem. Soc.*, **164**(11), E3613 (2017).
- Y. Orikasa, Y. Gogyo, H. Yamashige, M. Katayama, K. Chen, T. Mori, K. Yamamoto, T. Mase, Y. Inada, T. Ohta, Z. Siroma, S. Kato, H. Kinoshita, H. Arai, Z. Ogumi, and Y. Uchimoto, *Sci. Rep.*, **6**, 26382 (2016).
- P. Pietsch and V. Wood, *Annu. Rev. Mater. Res.*, **47**(1), 451 (2017).
- P. R. Shearing, N. P. Brandon, J. Gleb, R. Bradley, P. J. Withers, A. J. Marquis, S. Cooper, and S. J. Harris, *J. Electrochem. Soc.*, **159**(7), A1023 (2012).
- M. Ender, J. Joos, and T. Carraro, and E. Ivers-Tiffée, *J. Electrochem. Soc.*, **159**(7), A972 (2012).
- M. Ebner, F. Geldmacher, F. Marone, M. Stampanoni, and V. Wood, *Adv. Energy Mater.*, **3**(7), 845 (2013).
- S. Cooper, D. Eastwood, J. Gelb, G. Damblanc, D. Brett, R. Bradley, P. Withers, P. Lee, A. Marquis, N. Brandon, and P. Shearing, *J. Power Sources*, **247**(0), 1033 (2014).
- F. Tariq, V. Yufit, M. Kishimoto, P. Shearing, S. Menkin, D. Golodnitsky, J. Gelb, E. Peled, and N. Brandon, *J. Power Sources*, **248**, 1014 (2014).
- O. O. Taiwo, D. P. Finegan, D. S. Eastwood, J. L. Fife, L. D. Brown, J. A. Darr, P. D. Lee, D. J. L. Brett, and P. R. Shearing, *J. Microsc.*, **263**(3), 280 (2016).
- G. J. Nelson, L. J. Ausderau, S. Shin, J. R. Buckley, A. Mistry, P. P. Mukherjee, and V. De Andrade, *J. Electrochem. Soc.*, **164**(7), A1412 (2017).
- S. R. Daemi, C. Tan, T. Volkenandt, S. J. Cooper, A. Palacios-Padros, J. Cookson, D. J. L. Brett, and P. R. Shearing, *ACS Appl. Energy Mater.* (2018).
- D. E. Stephenson, B. C. Walker, C. B. Skelton, E. P. Gorzkowski, D. J. Rowenhorst, and D. R. Wheeler, *J. Electrochem. Soc.*, **158**(7), A781 (2011).
- S. W. Peterson and D. R. Wheeler, *J. Electrochem. Soc.*, **161**(14), A2175 (2014).
- T. Hutzenlaub, S. Thiele, N. Paust, R. Spotnitz, R. Zengerle, and C. Walchshofer, *Electrochim. Acta*, **115**(0), 131 (2014).
- C. Lim, B. Yan, H. Kang, Z. Song, W. C. Lee, V. De Andrade, F. De Carlo, L. Yin, Y. Kim, and L. Zhu, *J. Power Sources*, **328**, 46 (2016).
- S. A. Roberts, V. E. Brunini, K. N. Long, and A. M. Grillet, *J. Electrochem. Soc.*, **161**(11), F3052 (2014).
- H. Mendoza, S. A. Roberts, V. E. Brunini, and A. M. Grillet, *Electrochim. Acta*, **190**, 1 (2016).
- D. S. Eastwood, V. Yufit, J. Gelb, A. Gu, R. S. Bradley, S. J. Harris, D. J. L. Brett, N. P. Brandon, P. D. Lee, P. J. Withers, and P. R. Shearing, *Adv. Energy Mater.*, **4**(4), 1300506 (2014).
- D. P. Finegan, E. Tudisco, M. Scheel, J. B. Robinson, O. O. Taiwo, D. S. Eastwood, P. D. Lee, M. D. Michiel, B. Bay, S. A. Hall, G. Hinds, D. J. L. Brett, and S. P. R. Adv. Sci., **3**, 1500332 (2016).
- J. M. Paz-Garcia, O. O. Taiwo, E. Tudisco, D. P. Finegan, P. R. Shearing, D. J. L. Brett, and S. A. Hall, *J. Power Sources*, **320**, 196 (2016).
- S. Jaiser, J. Kumberg, J. Klaver, J. L. Urai, W. Schabel, J. Schmatz, and P. Scharfer, *J. Power Sources*, **345**, 97 (2017).
- L. Zielke, T. Hutzenlaub, D. R. Wheeler, I. Manke, T. Arlt, N. Paust, R. Zengerle, and S. Thiele, *Adv. Energy Mater.*, **4**(8), (2014).
- M. M. Forouzan, C.-W. Chao, D. Bustamante, B. A. Mazzeo, and D. R. Wheeler, *J. Power Sources*, **312**, 172 (2016).
- S. A. Roberts, H. Mendoza, V. E. Brunini, and D. R. Noble, *J. Comp. Phys.*, **375**, 352 (2018).
- D. Kehrwald, P. R. Shearing, N. P. Brandon, P. K. Sinha, and S. J. Harris, *J. Electrochem. Soc.*, **158**, A1393 (2011).
- A. M. Grillet, T. Humplik, E. K. Stirrup, S. A. Roberts, D. A. Barringer, C. M. Snyder, M. R. Janvrin, and C. A. Applett, *J. Electrochem. Soc.*, **163**(9), A1859 (2016).
- M. Stein, A. Mistry, and P. P. Mukherjee, *J. Electrochem. Soc.*, **164**(7), A1616 (2017).
- J. N. Israelachvili, *Intermolecular and Surface Forces*, Academic Press (2011).
- S. A. Roberts, H. Mendoza, V. E. Brunini, B. L. Trembacki, D. R. Noble, and A. M. Grillet, *J. Electrochem. Energy Convers. Storage*, **13**(3), 031005 (2016).
- D. R. Noble, E. P. Newren, and J. B. Lechman, *Int. J. Numer. Meth. Fluids*, **63**(6), 725 (2010).
- R. M. J. Kramer and D. R. Noble, *Int. J. Numer. Meth. Engng.* (2014).
- S. Torquato, *Random heterogeneous materials: microstructure and macroscopic properties*, volume 16. Springer Science & Business Media (2013).
- J. Huang and J. Zhang, *J. Electrochem. Soc.*, **163**(9), A1983 (2016).
- J. Newman and K. E. Thomas-Alyea, *Electrochemical systems*, John Wiley & Sons (2012).
- M. Ebner and V. Wood, *J. Electrochem. Soc.*, **162**(2), A3064 (2015).
- I. V. Thorat, D. E. Stephenson, N. A. Zacharias, K. Zaghbi, J. N. Harb, and D. R. Wheeler, *J. Power Sources*, **188**(2), 592 (2009).
- A. Vadakkepatt, B. Trembacki, S. R. Mathur, and J. Y. Murthy, *J. Electrochem. Soc.*, **163**(2), A1 (2016).

52. M. Ebner, D.-W. Chung, R. E. Garca, and V. Wood, *Adv. Energy Mater.*, **4**(5), 1301278 (2014).
53. V. D. Bruggeman, *Annalen der Physik*, **416**(7), 636 (1935).
54. M. Doyle, T. F. Fuller, and J. Newman, *J. Electrochem. Soc.*, **140**(6), 1526 (1993).
55. H. Zheng, J. Li, X. Song, G. Liu, and V. S. Battaglia, *Electrochim. Acta*, **71**, 258 (2012).
56. G. Liu, H. Zheng, A. S. Simens, A. M. Minor, X. Song, and V. S. Battaglia, *J. Electrochem. Soc.*, **154**(12), A1129 (2007).
57. B. J. Lanterman, A. A. Riet, N. S. Gates, J. D. Flygare, A. D. Cutler, J. E. Vogel, D. R. Wheeler, and B. A. Mazzeo, *J. Electrochem. Soc.*, **162**(10), A2145 (2015).
58. J. Landesfeind, J. Hattendorff, A. Ehrl, W. A. Wall, and H. A. Gasteiger, *J. Electrochem. Soc.*, **163**(7), A1373 (2016).
59. S. Patankar, *Numerical Heat Transfer and Fluid Flow*, CRC Press (1980).
60. H. K. Versteeg and W. Malalasekera, *An Introduction to Computational Fluid Dynamics: the Finite Volume Method*, Pearson Education (2007).
61. T. J. Hughes, *The finite element method: linear static and dynamic finite element analysis*, Courier Corporation (2012).
62. SIERRA Thermal/Fluid Development Team. SIERRA Multimechanics Module: Aria user manual - Version 4.46. Technical Report SAND2017-10427, Sandia National Laboratories (2017).
63. T. Hutzenlaub, A. Asthana, J. Becker, D. Wheeler, R. Zengerle, and S. Thiele, *Electrochem. Commun.*, **27**, 77 (2013).
64. J. Landesfeind, M. Ebner, A. Eldiven, V. Wood, and H. A. Gasteiger, *J. Electrochem. Soc.*, **165**(3), A469 (2018).
65. B. G. Westphal and A. Kwade, *J. Energy Storage*, **18**, 509 (2018).
66. M. Soderberg and G. Grimvall, *J. Phys. C: Solid State Phys.*, **16**(6), 1085 (1983).
67. A. Wiegmann, Geodict virtual microstructure simulator and material property predictor. <https://www.math2market.com> (2011).